

# Chapter 5

## 3-D Results

### 5.1 CGG Green Canyon IV 3-D Data

In 2003, CGG donated a large portion of a 161-block speculative seismic survey it acquired in the Green Canyon region of the Gulf of Mexico. The data were acquired in the transition zone between the edge of the Continental Shelf and the Sigsbee escarpment which signals the edge of the abyssal plain. Geologically, the Green Canyon region is characterized by sedimentary “minibasins” interrupted by complex salt bodies (AAPG, 1998).

CGG’s 3-D data were acquired by a ship sailing east-to-west, in the strike direction relative to the dominant geologic dip. The subset of the data that I process in this thesis contain fairly significant crossline dip ( $> 3^\circ$ ) in most places. Figure 5.1 shows a stacked section of the subset, which contains 192 midpoints inline and 14 midpoints crossline. The stacked section includes contributions from two adjacent sail lines, the geometry of which is illustrated in Figure 5.2.

The subset shown in Figure 5.1 is situated in a sedimentary minibasin, with strong reflections visible at a two-way traveltime of well over 5 seconds. Thanks to a strong velocity gradient and the sparse offset sampling, surface-related multiples are largely absent from the stacked section. Still, as we shall see, the multiples are fairly strong in the prestack data, and would likely inhibit prestack amplitude analysis. The section exhibits moderate reflector dip,

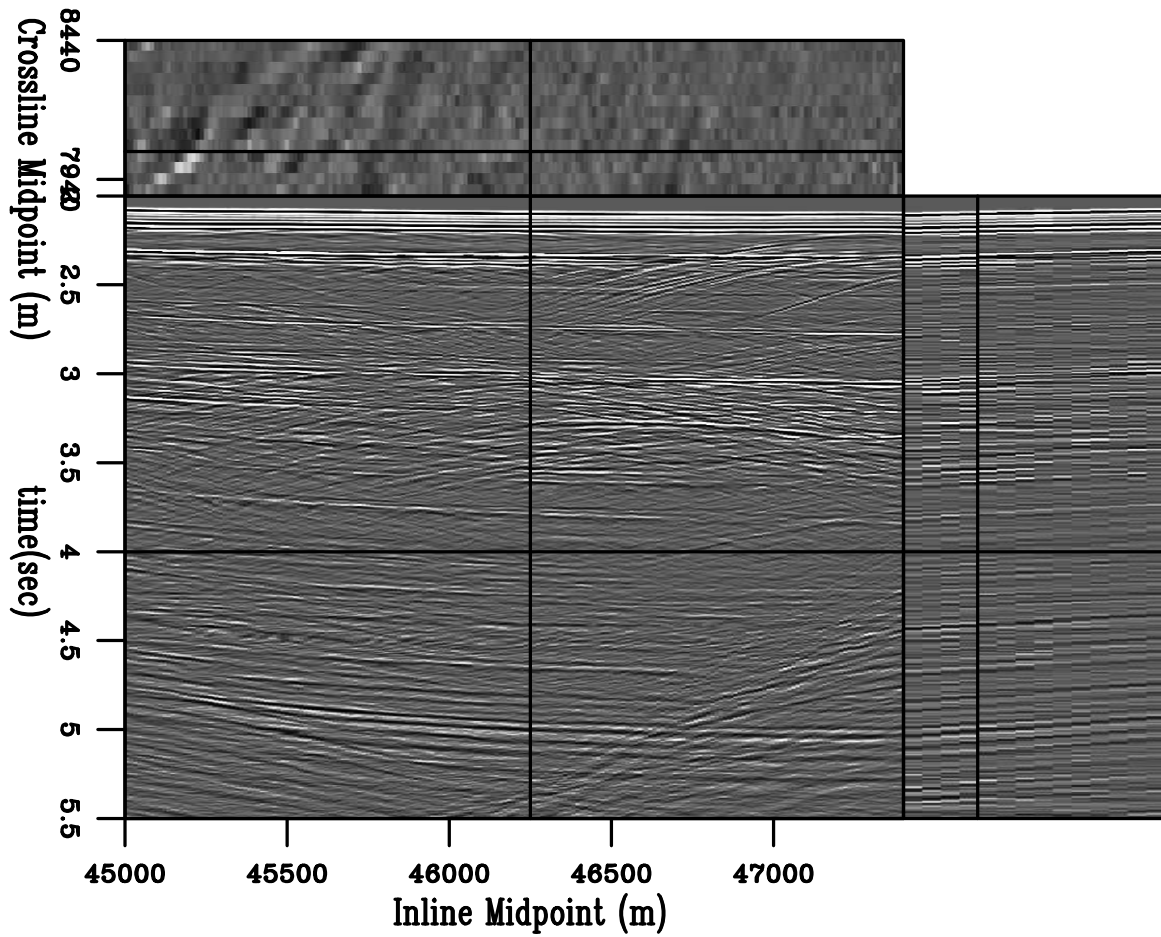


Figure 5.1: Stacked section of subset of Green Canyon IV 3-D dataset processed in this chapter. `results3d-stackraw3d.gc3d` [ER]

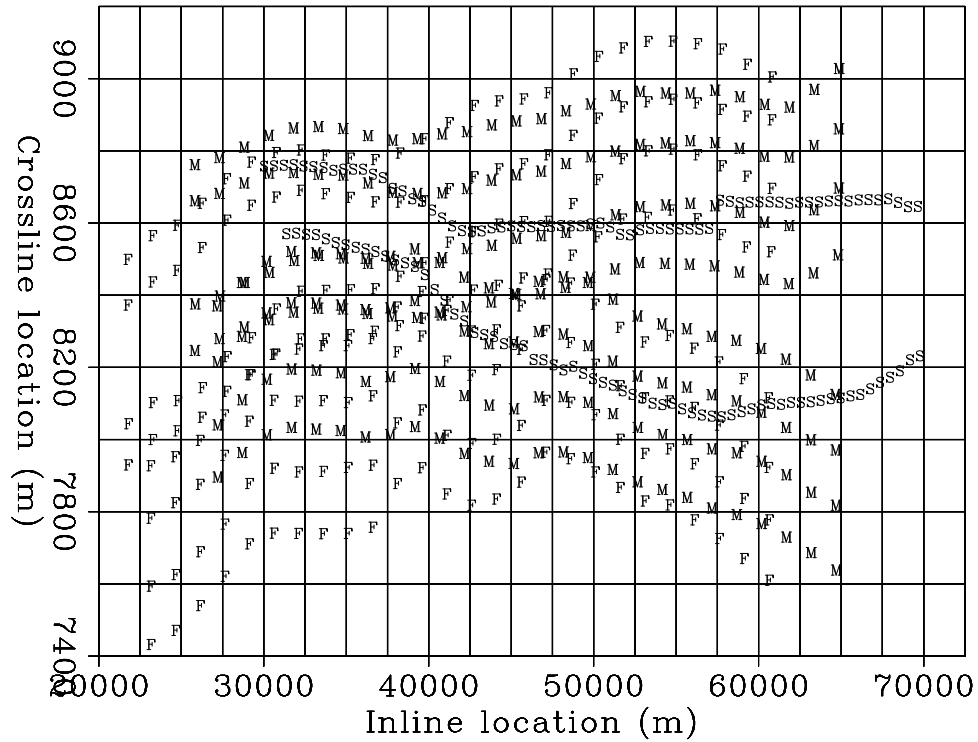


Figure 5.2: Acquisition geometry for two sail lines contributing to subset shown in Figure 5.1. “S” symbols illustrate source positions. “M” and “F” symbols illustrate the medium- and far-offset receivers, respectively, on each of the boat’s four streamers. The nominal sail line spacing is 300 meters, although it varies considerably in this case from about 200 to 500 meters. The subset processed in this section contains shot records from about 40,000 to 50,000 meters inline location. Cable feathering in this zone is present, though not severe. Although they are not supposed to, the two sail lines overlap to some extent, which reduces the number of crossline midpoint locations from these two sail lines to 14 from 16 over the subset. `results3d-feather` [NR]

from an anticlinal structure in the inline direction and an effectively constant crossline dip of several degrees.

The acquisition ship sailed quite fast, with a flip-flop source interval of 37.5 meters, and an interval of 75 meters between like sources. The fast ship speed leads to reduced resolution along the inline offset axis: for an 8100-meter cable with receiver group spacing of 25 meters, the nominal fold is only 54, implying a nominal inline offset spacing of 150 meters. Figure 5.3 illustrates the sparse sampling of the inline offset axis. While the nominal inline offset bin size of 150 meters ensures that all bins will contain a live trace, such sparsity will greatly inhibit the estimation of reasonable stacking velocities and create “checkerboard” artifacts in the shallow portions of a stacked image.

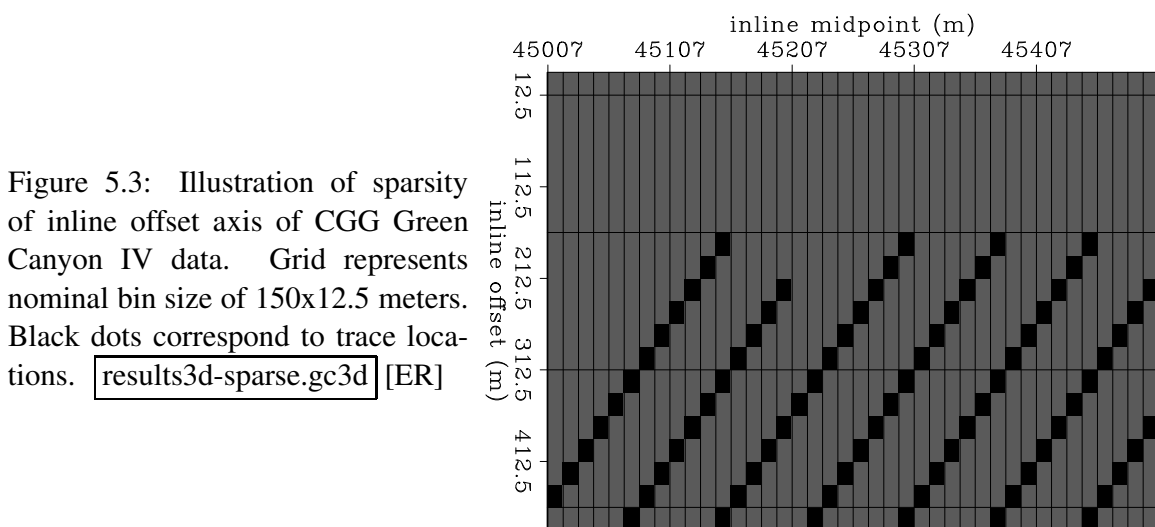


Figure 5.3: Illustration of sparsity of inline offset axis of CGG Green Canyon IV data. Grid represents nominal bin size of 150x12.5 meters. Black dots correspond to trace locations. `results3d-sparse.gc3d` [ER]

Therefore, in my processing of this dataset, I use an offset bin spacing of 25 meters. While this fine sampling better honors the physics of the experiment, it leads to a fivefold increase in empty bins. Moreover, although I have cast LSJIMP primarily as a wavefield separation algorithm, recall that one major motivation of integrating multiples and primaries is to use the multiples as a constraint on the primaries in zones where we do not record data. Multiples sample reflectors more finely in reflection angle/offset than do primaries. Moreover, the regularization strategies presented in Section 2.1.3 provide the infrastructure to exploit the inherent multiplicity of signal within an image and between multiple and primary images. Although designed to separate signal and noise, these same strategies also prove adept at interpolating

signal in missing traces.

Stacking velocities were computed by a conventional velocity scan, coupled with maximum amplitude autopicking and local weighted (stack power) mean smoothing. The residual weight, simply zero for missing traces, but one elsewhere, is particularly important to achieve a successful LSJIMP result.

## 5.2 Results

Figure 5.4 shows stacked sections from the multiple-infested zone of the CGG subset before and after application of LSJIMP. Figure 5.5 is in the same format, but shows a zoom of the multiple-infested region. CMP stacking strongly suppresses the multiples, but from the difference panel, notice that LSJIMP has nonetheless subtracted most of the remaining surface-related multiple energy, and has preserved the stronger primaries to a great extent. The timeslice on the 3-D cube transects the seabed pegleg from reflector R1; it shows up prominently on the raw data stack, as well as on the difference panel, but has been largely suppressed from the LSJIMP estimated primaries stack.

Figures 5.6 and 5.7 illustrate LSJIMP's performance on two individual CMP gathers extracted from different portions of the CGG 3-D data. It is in this domain where the strength of the LSJIMP method shines most. The raw data panels show strong surface-related multiples with an onset of around 4.3 seconds, and also fairly strong primary events under the curtain of multiples. The LSJIMP estimated primaries in panel (b) are effectively free of multiples, and moreover, since the data residual panel (f) barely contains any noticeable flat primary energy, we have preserved the primary events. Also notice that the data residual contains little structured energy. This implies that the LSJIMP forward model accurately models the primaries and important multiples in the data. Unfortunately, much of this "unstructured" energy likely belongs to fairly weak pegleg multiples that simply appear incoherent with the data's poor inline resolution. On Figure 5.7, notice that cable feathering has caused missing traces at far offsets. LSJIMP has used the data's multiplicity and model constraints to reasonably extrapolate the missing traces.

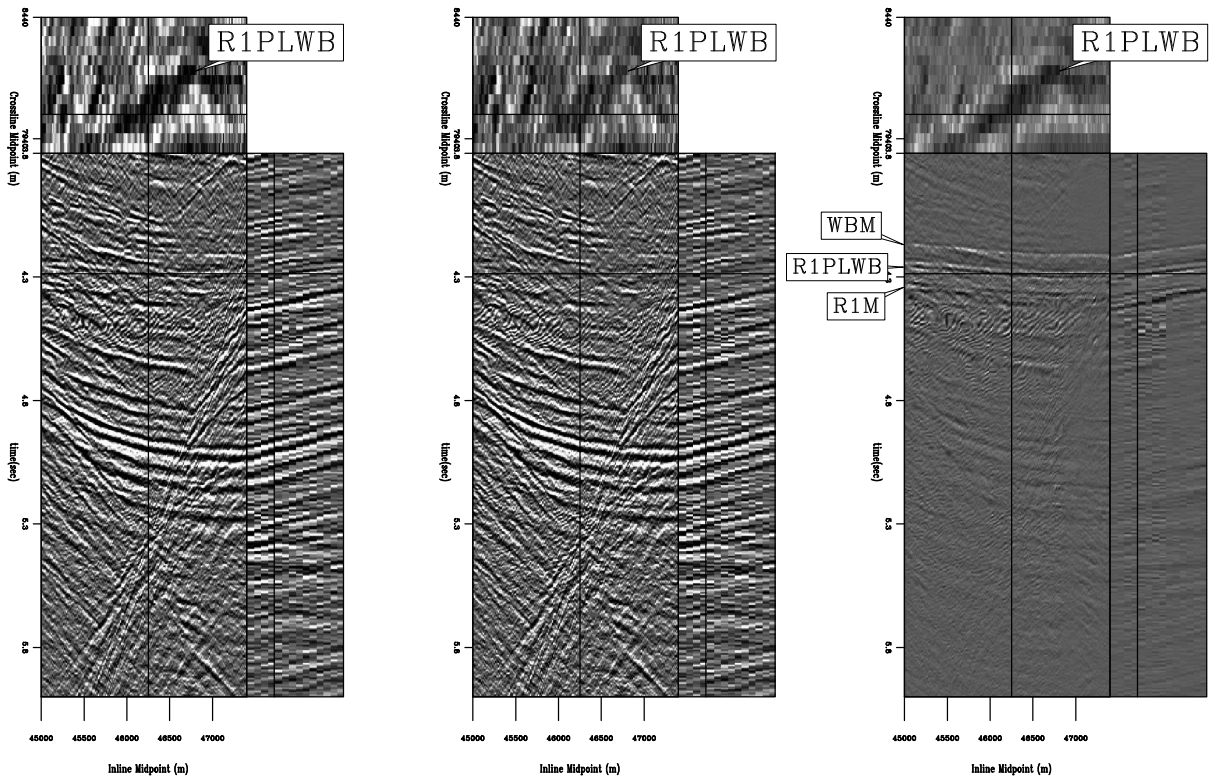


Figure 5.4: Stacked subset (192 midpoints inline, 14 midpoints crossline) of CGG 3-D data before and after LSJIMP. All panels windowed in time from 3.8 to 6.0 seconds and gained with  $t^2$ . Left: Raw data stack. Center: Stack of estimated primary image,  $\mathbf{m}_0$ . Right: Stack of the subtracted multiples. Naming convention for pure first-order multiples: (*reflector*)M, e.g., R1M. Naming convention for first-order pegleg multiples: (*target*)PL(*multiple generator*), e.g., R1PLWB. `results3d-stackcomp3d.gc3d` [CR,M]

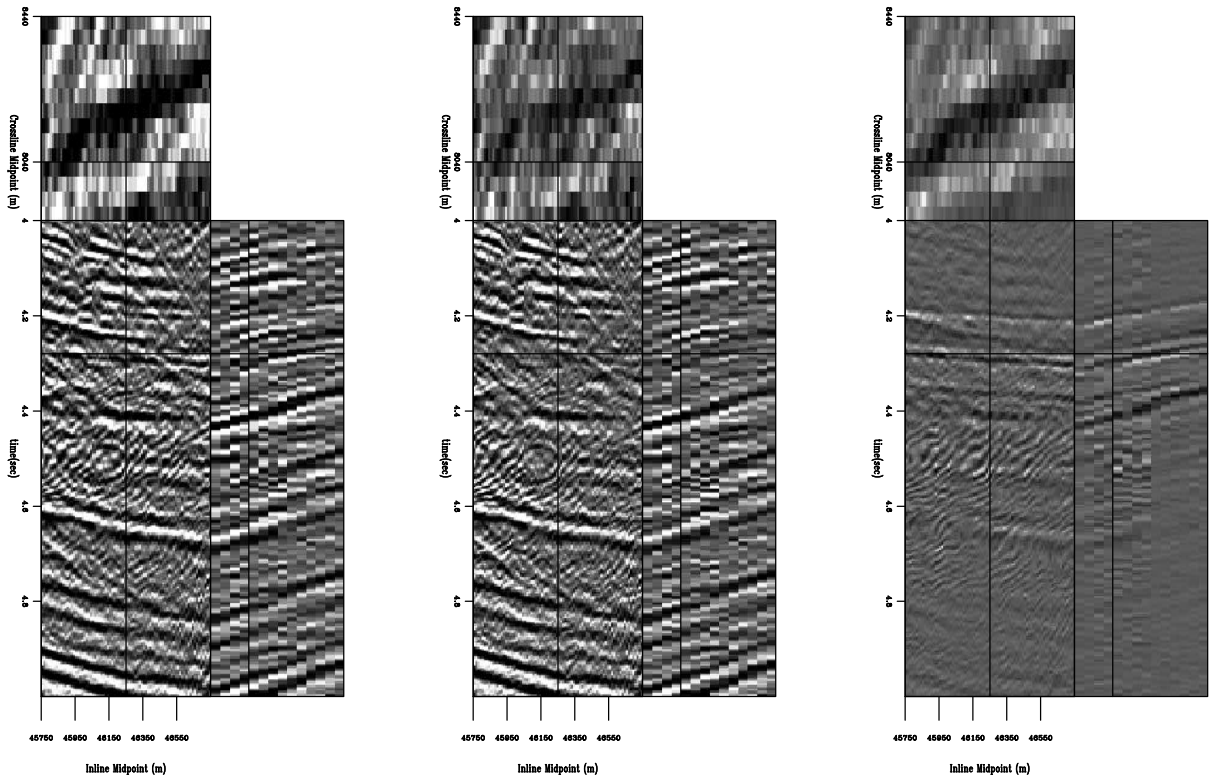


Figure 5.5: Zoom of stacked subset of CGG 3-D data before and after LSJIMP. All panels windowed in time from 4.0 to 5.0 seconds. Left: Raw data stack. Center: Stack of estimated primary image,  $\mathbf{m}_0$ . Right: Stack of the subtracted multiples. `results3d-stackcomp3d.zoom.gc3d` [CR,M]

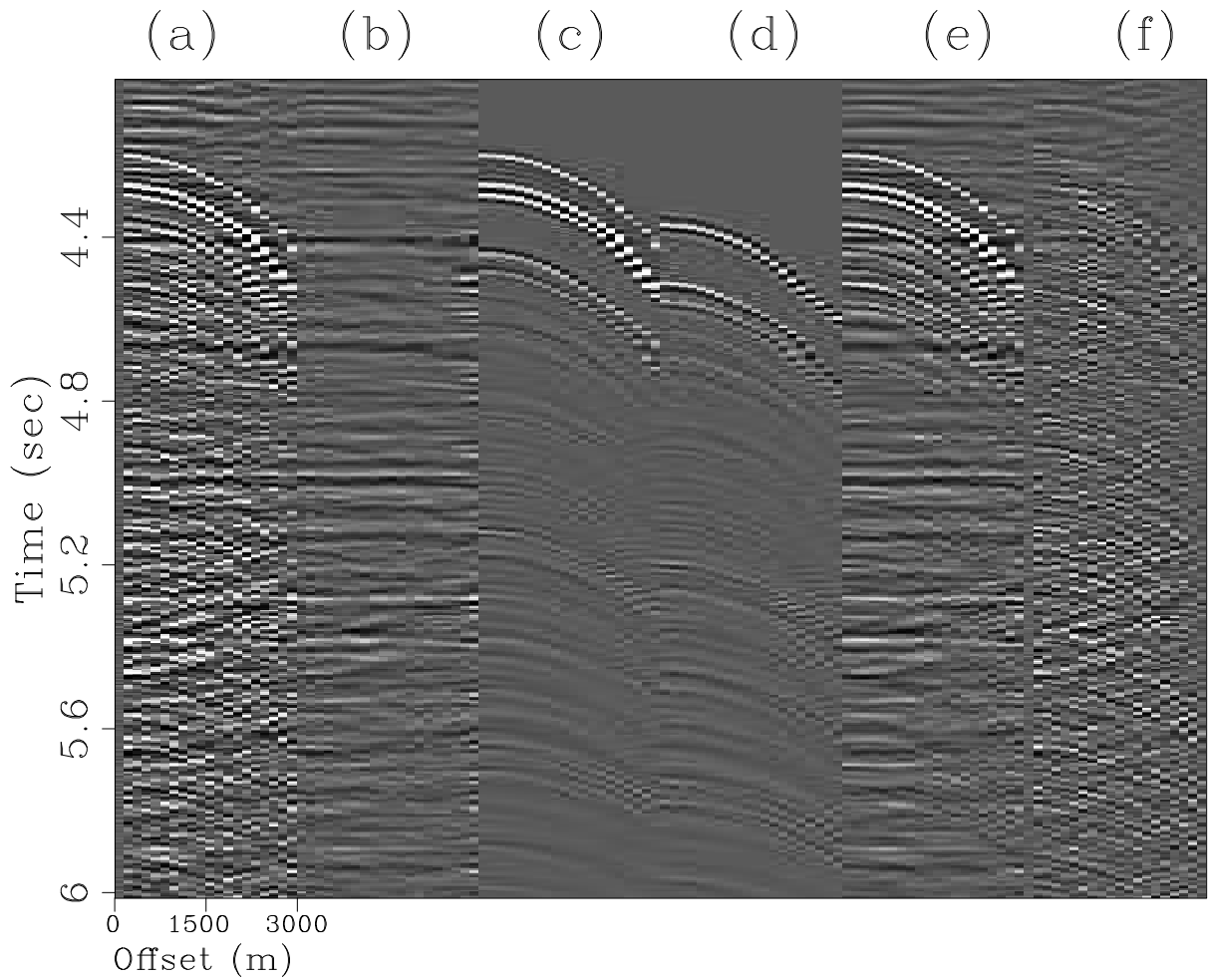


Figure 5.6: LSJIMP results on individual midpoint location ( $CMP_x=100, CMP_y=4$ ). All panels decimated in offset by a factor of 6 and NMO'ed with stacking velocity, for display purposes. Panel (a): Raw data. Panel (b): LSJIMP estimated primaries. Panels (c) and (d): Estimated seabed and R1 pegleg multiples. Panel (e): Modeled data (sum of panels (b), (c), and (d)). Panel (f): Data residual (difference of panels (a) and (e)), with residual weight applied. `results3d-compwind.lsrow.gc3d.100.4` [CR]

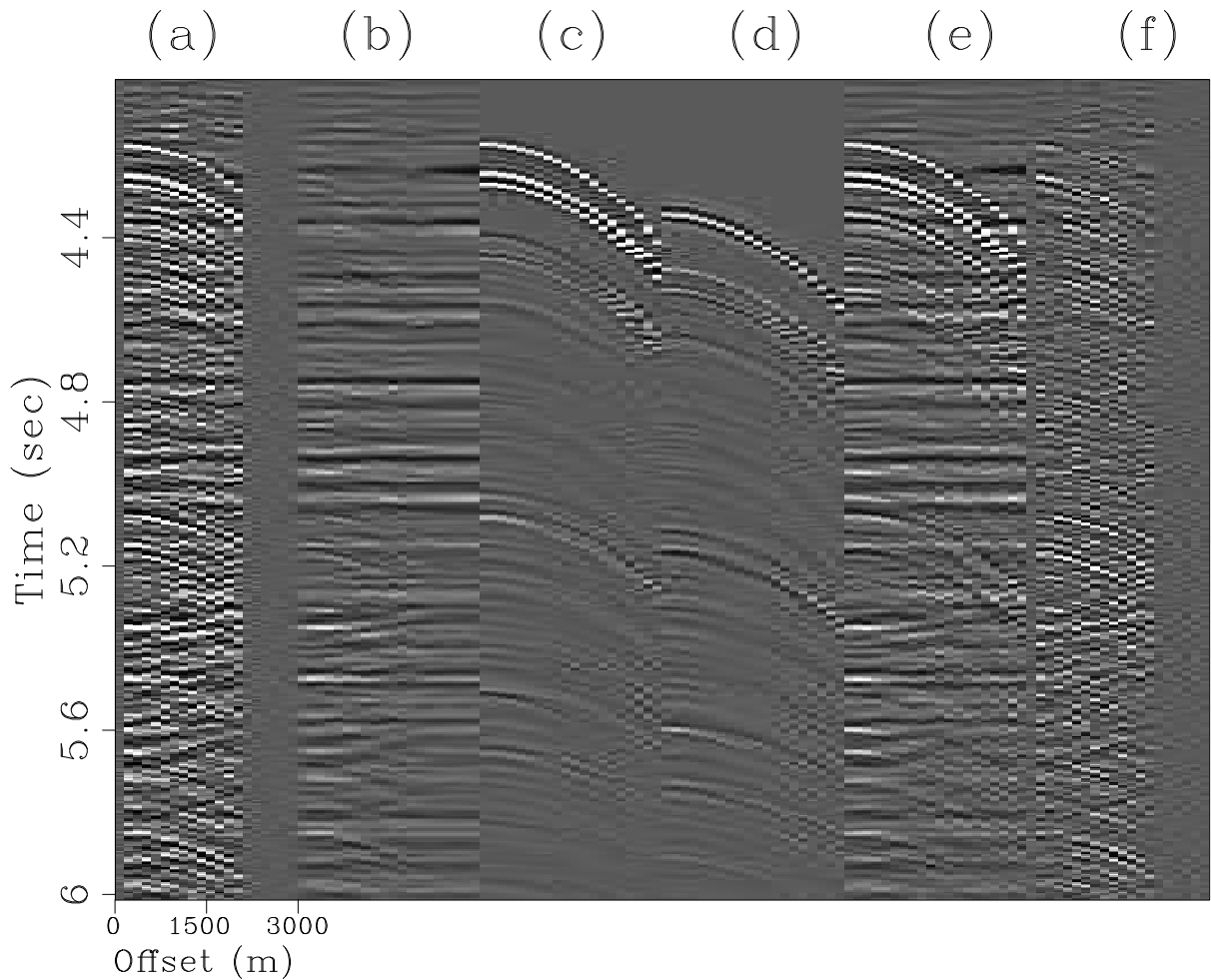


Figure 5.7: LSJIMP results on individual midpoint location ( $CMP_x=100, CMP_y=12$ ). All panels decimated in offset by a factor of 6 and NMO'ed with stacking velocity, for display purposes. Panel (a): Raw data. Panel (b): LSJIMP estimated primaries. Panels (c) and (d): Estimated seabed and R1 pegleg multiples. Panel (e): Modeled data (sum of panels (b), (c), and (d)). Panel (f): Data residual (difference of panels (a) and (e)), with residual weight applied. `results3d-compwind.lsrow.gc3d.100.12` [CR]

### 5.2.1 LSJIMP versus Radon Demultiple

Radon demultiple remains the default multiple suppression technique in many situations, particularly in 3-D, where acquisition sparsity may inhibit other techniques. On CMP gathers, primaries and multiples normally have different apparent velocities, and a Radon transform which sums across offset using various curvature parameters will focus the two types of events in different parts of the transform panel. The most natural curvature parameter for CMP data is the velocity of the hyperbola defined by the NMO equation (2.16) (Foster and Mosher, 1992). While the Hyperbolic Radon transform is a linear mapping, it is not time-invariant, and thus cannot be implemented efficiently as a Fourier domain operator. However, a multiple's residual moveout after NMO is approximately parabolic (quadratic) with offset, so a time-invariant Parabolic Radon transform is much faster, though not as accurate (Hampson, 1986; Kabir and Marfurt, 1999).

To remove multiples, the primary energy in the transform panel is muted, and the inverse radon transform applied to produce an estimate of the multiples, which is subtracted from the data to produce a primary estimate. If we define  $\mathbf{d}$  as a raw CMP gather,  $\mathbf{H}$  as the linear mapping between radon transform space and data space,  $\mathbf{M}$  as a mute operator that zeroes primary energy in radon transform space, and  $\mathbf{d}_r$  as the estimated primaries, then we can express the radon demultiple process in equation form:

$$\mathbf{d}_r = \mathbf{H}\mathbf{M}^T\mathbf{H}^T\mathbf{d}. \quad (5.1)$$

Operator  $\mathbf{H}$  is non-unitary ( $\mathbf{H}^T\mathbf{H} \neq \mathbf{I}$ ), so the amplitude of the estimated primaries will not match the recorded primaries. By casting Radon demultiple as a least-squares optimization problem, the Radon transform panel can be scaled such that  $\mathbf{d}_r$  and  $\mathbf{d}$  are directly comparable. We first optimize a Radon transform panel,  $\mathbf{p}$ , to minimize the data misfit:

$$\min_{\mathbf{p}} Q(\mathbf{p}) = \|\mathbf{H}\mathbf{p} - \mathbf{d}\|^2, \quad (5.2)$$

and then apply the mute operator and adjoint of  $\mathbf{H}$  to produce the estimated primaries:

$$\mathbf{d}_r = \mathbf{d} - \mathbf{H}\mathbf{M}^T \mathbf{p}. \quad (5.3)$$

The finite frequency content of the data, limited extent of the array, and the intrinsic unresolvability of velocity information at zero offset all contribute to the non-uniqueness of the least-squares Radon demultiple problem. At far offsets, events with many zero-offset traveltimes and different velocities are fit equally well by a single curvature parameter. Low-frequency data makes moveout discrimination between multiples and primaries more difficult. At near offsets, all the events are fit equally well by all curvature parameters. All these pitfalls lead to reduced resolution of events in the Radon domain. So-called “high resolution” least-squares Radon transform implementations partially overcome these problems by imposing sparsity constraints in either the hyperbolic or parabolic Radon domain (Thorson and Claerbout, 1985; Sacchi and Ulrych, 1995).

I implemented and tested least-squares Hyperbolic Radon demultiple (LSHRTD) on the CGG 3-D data subset. I performed 10 conjugate gradient iterations to produce an optimal  $\mathbf{p}$ , then applied a mute function which is zero for velocities greater than 90% known stacking velocity. The mute tapers linearly from 1.0 to 0.0 between 85% and 90% of the stacking velocity. The computational cost of LSHRTD is very similar to the cost of applying LSJIMP.

Figure 5.8 compares the results of applying LSJIMP and LSHRTD on a single CMP gather from the CGG 3-D data ( $\text{CMP}_x=100$ ,  $\text{CMP}_y=4$ ). The LSHRTD results are quite good, as we expect, given the high velocity gradient and relatively simple moveout seen in this region of the data. Spatial aliasing causes some artifacts on the LSHRTD primaries (Figure 5.8(b)), around  $\tau = 4.4$  seconds. The radon primaries seem to contain a bit more spatially uncorrelated noise than the LSJIMP primaries. LSJIMP is a more “surgical” separation technique, although the model regularization operators also exploit moveout differences to separate multiples and primaries.

Figure 5.9, a stack of the LSHRTD estimated primaries, can be compared directly with the LSJIMP result, Figure 5.5. Like before, the multiples predominantly stack out, since the moveout separation is so significant. Still, a noticeable amount of multiple energy has been

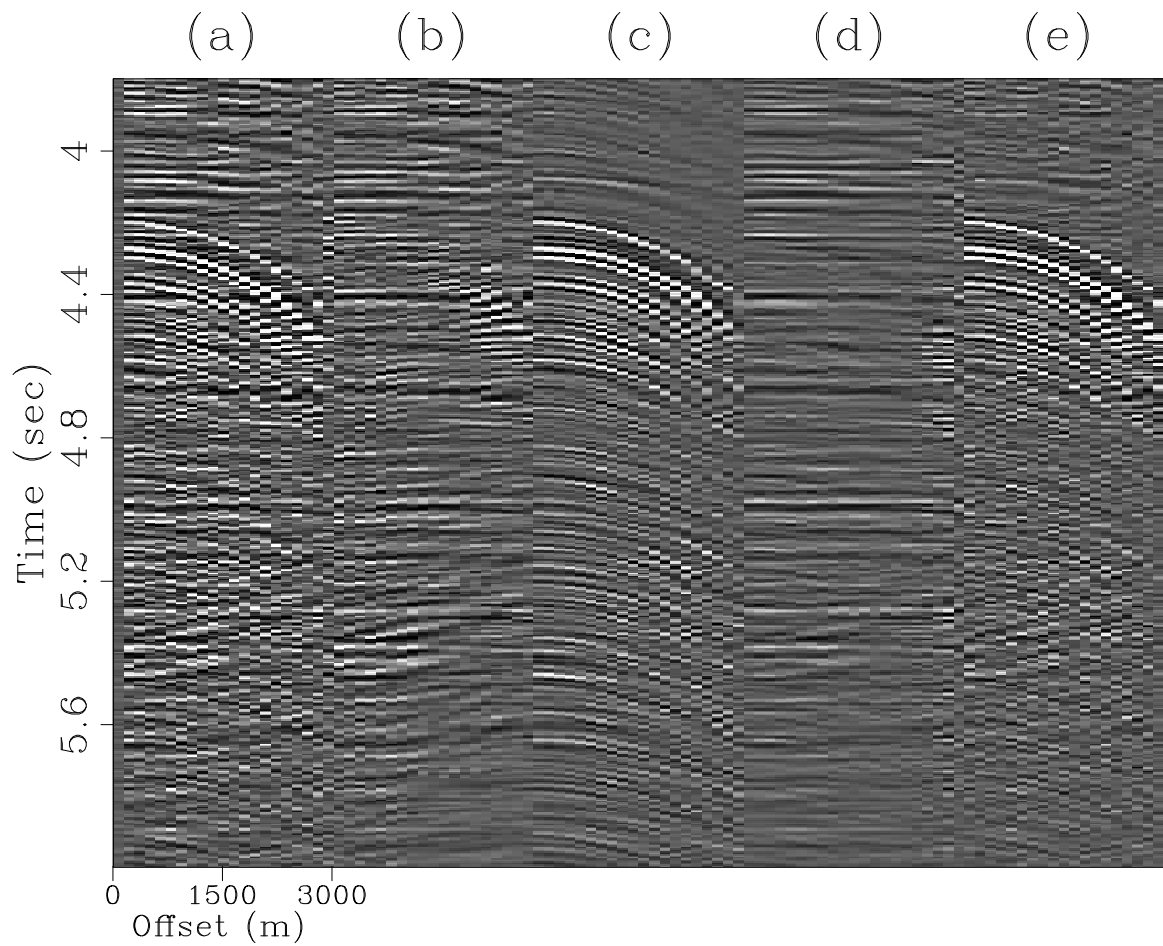


Figure 5.8: LSJIMP versus least-squares Hyperbolic Radon demultiple (LSHRTD) on one CMP gather of the CGG 3-D dataset. Panel (a): Raw data. Panel (b): LSHRTD estimated primaries. Panel (c): LSHRTD estimated multiples. Panel (d): LSJIMP estimated primaries. Panel (e): LSJIMP estimated multiples. `results3d-comp.radon.gc3d.100` [CR]

removed by LSHRTD, perhaps more than by LSJIMP. However, we immediately see some removed primary energy: for example, the strong primary near the bottom of the section.

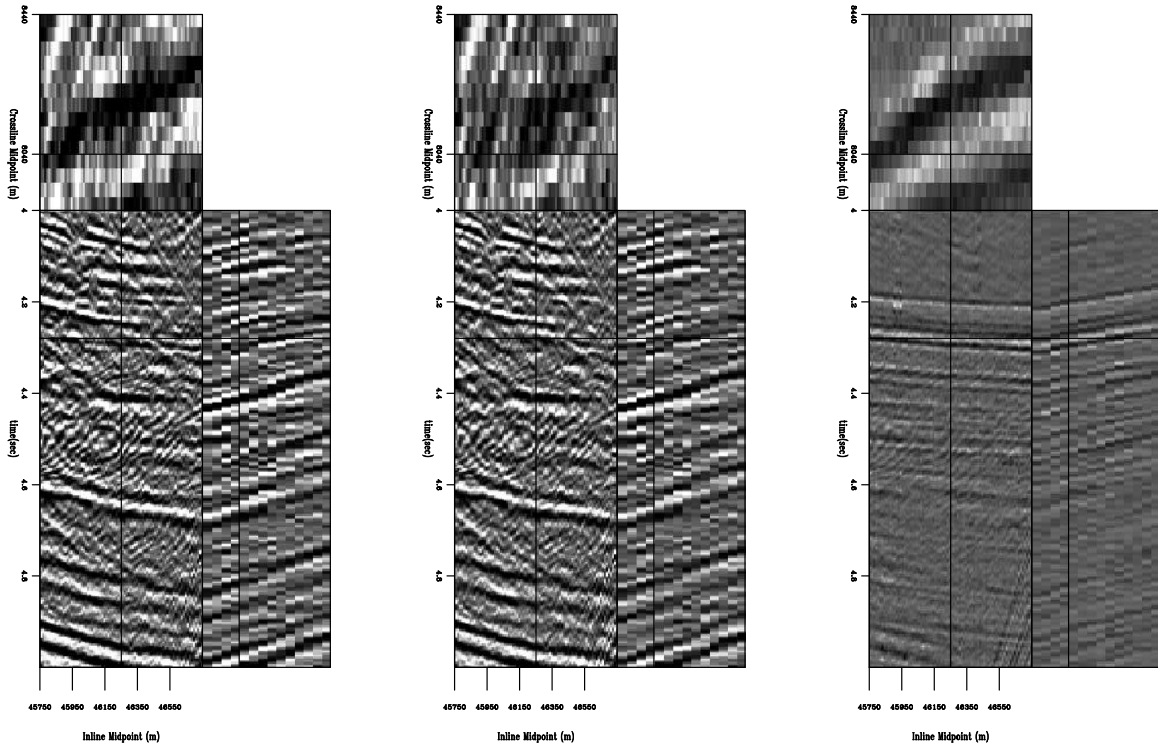


Figure 5.9: NMO/Stack comparison before and after LSHRTD. Compare directly with Figure 5.5. Left: Raw data. Center: LSHRTD estimated primaries. Right: difference. `results3d-stackcomp3d.radon.zoom.gc3d` [CR,M]

## 5.2.2 AVO Analysis Before and After LSJIMP

Amplitude-versus-offset or AVO analysis is perhaps the most commonly utilized direct hydrocarbon indicator in exploration reflection seismology today. The stacked results before and after LSJIMP on the Green Canyon 3-D dataset showed that stacking greatly attenuates multiples. However, from the prestack data, we saw that the multiples are prominent, and would surely inhibit signal processing techniques, like AVO analysis, if left intact. In this section, I illustrate how LSJIMP improves the AVO analysis of the Green Canyon 3-D data.

Shuey (1985) showed that in a 1-D earth, the measured reflection strength of an event at the surface is approximately linear with the square of its incidence angle, at angles less than 30 degrees. In a 1-D earth, the NMO equation gives an approximate relationship between offset and incidence angle. Claerbout (1995) defines the “stepout”,  $p$ , as the spatial derivative of an event’s travelttime curve:

$$p = \frac{dt}{dx} = \frac{\sin\theta}{V}, \quad (5.4)$$

where  $\theta$  is the incidence angle and  $V$  is the velocity at the surface; in the marine case, simply water velocity. Stepout was earlier used to derive the Snell Resampling operator in Section 2.2.3. In a 1-D earth, the travelttime curve of a primary reflection is approximately given by the NMO equation (2.16). Taking the derivative of equation (2.16) with respect to offset, then substituting into equation (5.4) gives the following expression for the sine of incidence angle as a function of offset:

$$\sin\theta = \frac{V}{V_{\text{rms}}^2(\tau)} \frac{x}{\sqrt{\tau^2 + \frac{x^2}{V_{\text{rms}}^2(\tau)}}}. \quad (5.5)$$

Reflection data as a function of offset may be mapped to  $\sin^2\theta$  via equation (5.5), at which point the AVO “slope” and “intercept” parameters may be estimated, usually via a linear least-squares fit to the data after resampling from offset to  $\sin^2\theta$ .

Figure 5.10 illustrates the estimation of AVO slope and intercept parameters on a deep reflector in the Green Canyon 3-D data, before and after application of LSJIMP. The reflector, which is well under the multiples in the data, is denoted on the zero offset section with “O” symbols. The maximum amplitude in a small time window around the reflection were picked automatically, and make up the input data to the least-squares estimation.

We see that while the parameter estimates contain the same trends before and after LSJIMP, the LSJIMP result is more consistent and less “noisy” across midpoint. My implementation of LSJIMP works on a CMP-by-CMP basis, so the results shown in Figure 5.10 are not smoothed across midpoint. The similarity across midpoint is an expression of the true lithology – lithology which LSJIMP better reveals.

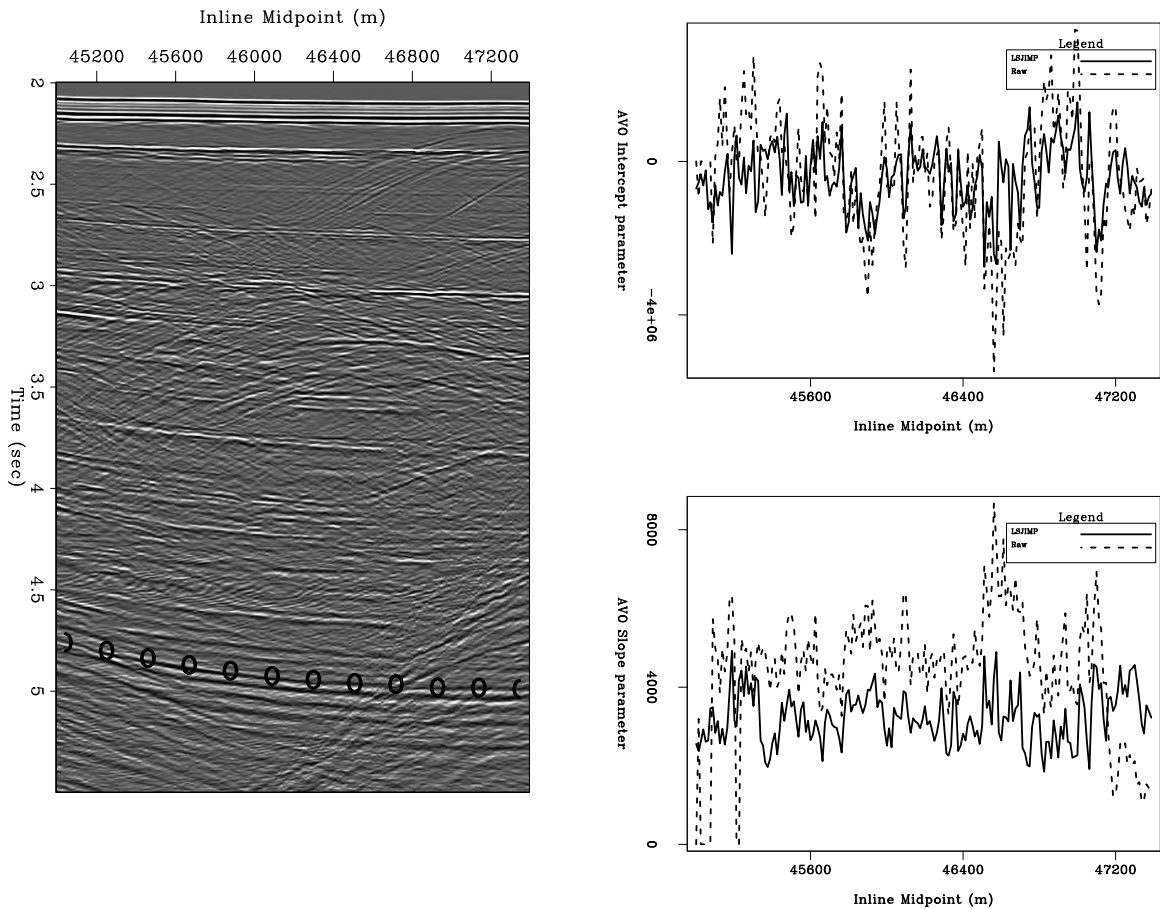


Figure 5.10: AVO parameter estimation for a deep reflector. Left: zero offset section, “O” symbols denote reflector of interest. Right, top: AVO intercept parameter before and after LSJIMP, as a function of midpoint. Right, bottom: AVO slope parameter before and after LSJIMP, as a function of midpoint. `results3d-maxampl.gc3d.4-5` [CR]

Figure 5.11 illustrates, as a function of midpoint, the small time windows taken around the deep reflector shown in Figure 5.10, before and after LSJIMP. The input data to an AVO parameter estimation are picked maximum amplitudes within the time window as a function of  $\sin^2\theta$ . Notice the significant increase in reflector clarity after LSJIMP. Also recall that the data residuals (e.g., in Figures 5.6 and 5.7) are quite small. Therefore, the cleaner reflection events after LSJIMP in Figure 5.11 are not only better for AVO analysis – they also fit the recorded data in a quantitative fashion. LSJIMP is not an *ad hoc* post-processing technique.

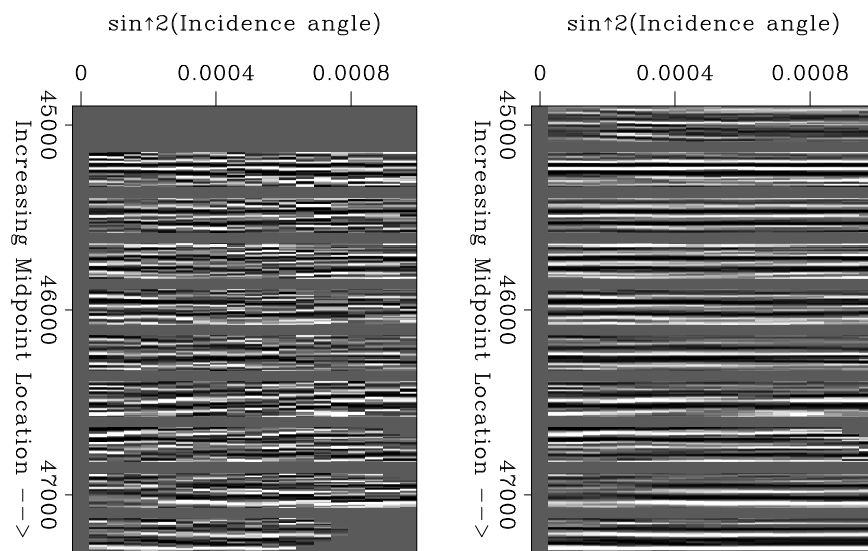


Figure 5.11: Small time windows around the deep reflector shown in Figure 5.10, before and after LSJIMP. Individual panels along the vertical axis correspond to windows taken at different midpoint locations. Left: Data windows before LSJIMP. Right: Data windows after LSJIMP. [results3d-avogather.gc3d.4-5](#) [CR]

# Bibliography

- AAPG, 1998, Gulf of Mexico petroleum systems: AAPG Bulletin, **82**, no. 5.
- Berkhout, A. J., and Verschuur, D. J., 1994, Multiple technology: Part 2, migration of multiple reflections: Soc. of Expl. Geophys., 64th Ann. Internat. Mtg, 1497–1500.
- Berkhout, A. J., and Verschuur, D. J., 2003, Transformation of multiples into primary reflections: *in* 73rd Ann. Internat. Mtg Soc. of Expl. Geophys.
- Berryhill, J. R., and Kim, Y. C., 1986, Deep-water peglegs and multiples - Emulation and suppression: Geophysics, **51**, no. 12, 2177–2184.
- Biondi, B., and Palacharla, G., 1996, 3-D prestack migration of common-azimuth data: Geophysics, **61**, no. 06, 1822–1832.
- Biondi, B., Fomel, S., and Chemingui, N., 1998, Azimuth moveout for 3-D prestack imaging: Geophysics, **63**, no. 02, 574–588.
- Biondi, B., 1997, Azimuth moveout + common-azimuth migration: Cost-effective prestack depth imaging of marine data: Soc. of Expl. Geophys., 67th Ann. Internat. Mtg, 1375–1378.
- Brown, M., 2002, Simultaneous estimation of two slopes from seismic data, applied to signal/noise separation: SEP-**112**, 181–194.
- Claerbout, J. F., 1992, Earth Soundings Analysis: Processing Versus Inversion: Blackwell Scientific Publications.

- Claerbout, J. F., 1995, Basic Earth Imaging: Stanford Exploration Project.
- Fomel, S., 2001, Three-dimensional seismic data regularization: Ph.D. thesis, Stanford University.
- Fomel, S., 2002, Applications of plane-wave destruction filters: *Geophysics*, **67**, no. 06, 1946–1960.
- Foster, D. J., and Mosher, C. C., 1992, Suppression of multiple reflections using the Radon transform: *Geophysics*, **57**, no. 03, 386–395.
- Guitton, A., Brown, M., Rickett, J., and Clapp, R., 2001, Multiple attenuation using a t-x pattern-based subtraction method: *Soc. of Expl. Geophys.*, 71st Ann. Internat. Mtg, 1305–1308.
- Guitton, A., 2002, Shot-profile migration of multiple reflections: 72nd Ann. Internat. Mtg., *Soc. of Expl. Geophys.*, Expanded Abstracts, 1296–1299.
- Hampson, D., 1986, Inverse velocity stacking for multiple elimination: *J. Can. Soc. Expl. Geophys.*, **22**, no. 01, 44–55.
- Hargreaves, N., Wombell, R., and VerWest, B., 2003, Multiple attenuation using an apex-shifted radon transform: 65th Mtg., *Eur. Assoc. Geosc. Eng.*, Workshop: Strategies Towards Multi-Dimensional Multiple Attenuation.
- He, R., and Schuster, G., 2003, Least-squares migration of both primaries and multiples: *in* 73rd Ann. Internat. Mtg Soc. of Expl. Geophys.
- Hokstad, K., and Sollie, R., 2003, 3-D surface-related multiple elimination using parabolic sparse inversion: *in* 73rd Ann. Internat. Mtg Soc. of Expl. Geophys., 1961–1964.
- Hutchinson, M., and De Hoog, F., 1985, Smoothing noisy data with spline functions: Smoothing noisy data with spline functions: *Numer. Math.*, 99–106.
- Kabir, M. M. N., and Marfurt, K. J., 1999, Toward true amplitude multiple removal: *The Leading Edge*, **18**, no. 1, 66–73.

- Kleemeyer, G., Pettersson, S., Eppenga, R., Haneveld, C., Biersteker, J., and Den Ouden, R., 2003, It's magic – industry first 3D surface multiple elimination and pre-stack depth migration on Ormen Lange.; *in* 65th Mtg. Eur. Assn. Geosci. Eng., Session:B–43.
- Kuehl, H., and Sacchi, M., 2001, Generalized least-squares DSR migration using a common angle imaging condition: Soc. of Expl. Geophys., 71st Ann. Internat. Mtg, 1025–1028.
- Levin, F. K., and Shah, P. M., 1977, Peg-leg multiples and dipping reflectors: *Geophysics*, **42**, no. 05, 957–981.
- Levin, F. K., 1971, Apparent velocity from dipping interface reflections: *Geophysics*, **36**, no. 03, 510–516.
- Levin, S. A., 1996, AVO estimation using surface-related multiple prediction: Soc. of Expl. Geophys., 66th Ann. Internat. Mtg, 1366–1369.
- Lomask, J., 2003, Flattening 3D seismic cubes without picking: Soc. of Expl. Geophys., 73rd Ann. Internat. Mtg., 1402–1405.
- Lu, G., Ursin, B., and Lutro, J., 1999, Model-based removal of water-layer multiple reflections: *Geophysics*, **64**, no. 6, 1816–1827.
- Morley, L., 1982, Predictive multiple suppression: Ph.D. thesis, Stanford University.
- Nemeth, T., Wu, C., and Schuster, G. T., 1999, Least-squares migration of incomplete reflection data: *Geophysics*, **64**, no. 1, 208–221.
- Ottolini, R., 1982, Migration of reflection seismic data in angle-midpoint coordinates: Ph.D. thesis, Stanford University.
- Paffenholz, J., 2003, All-azimuth streamer acquisition: the impact on 3D multiple attenuation: 65th Mtg., Eur. Assoc. Geosc. Eng., Workshop: Strategies Towards Multi-Dimensional Multiple Attenuation.
- Prucha, M. L., and Biondi, B. L., 2002, Subsalt event regularization with steering filters: 72nd Ann. Internat. Mtg., Soc. of Expl. Geophys., Expanded Abstracts, 1176–1179.

- Prucha-Clapp, M., and Biondi, B., 2002, Subsalt event regularization with steering filters: Soc. of Expl. Geophys., 72nd Ann. Internat. Mtg, 1176–1179.
- Reiter, E. C., Toksoz, M. N., Keho, T. H., and Purdy, G. M., 1991, Imaging with deep-water multiples: *Geophysics*, **56**, no. 07, 1081–1086.
- Rickett, J., and Lumley, D. E., 2001, Cross-equalization data processing for time-lapse seismic reservoir monitoring: A case study from the Gulf of Mexico: *Geophysics*, **66**, no. 4, 1015–1025.
- Riley, D. C., and Claerbout, J. F., 1976, 2-D multiple reflections: *Geophysics*, **41**, no. 04, 592–620.
- Ross, W. S., Yu, Y., and Gasparotto, F. A., 1999, Traveltime prediction and suppression of 3-D multiples: *Geophysics*, **64**, no. 1, 261–277.
- Sacchi, M. D., and Ulrych, T. J., 1995, High-resolution velocity gathers and offset space reconstruction: *Geophysics*, **60**, no. 04, 1169–1177.
- Sava, P., and Fomel, S., 2000, Angle-gathers by Fourier Transform: *SEP*–**103**, 119–130.
- Sava, P., and Fomel, S., 2003, Angle-domain common-image gathers by wavefield continuation methods: *Geophysics*, **68**, no. 3, 1065–1074.
- Shan, G., 2003, Source-receiver migration of multiple reflections:, *in* 73rd Ann. Internat. Mtg Soc. of Expl. Geophys.
- Shuey, R. T., 1985, A simplification of the Zoeppritz-equations: *Geophysics*, **50**, no. 04, 609–614.
- Stoffa, P. L., Fokkema, J. T., de Luna Freire, R. M., and Kessinger, W. P., 1990, Split-step Fourier migration: *Geophysics*, **55**, no. 4, 410–421.
- Taner, M. T., and Koehler, F., 1969, Velocity spectra - Digital computer derivation and applications of velocity functions: *Geophysics*, **34**, no. 06, 859–881.

- Taner, M. T., 1980, Long-period sea-floor multiples and their suppression: *Geophys. Prosp.*, **28**, no. 01, 30–48.
- Tarantola, A., 1984, Inversion of seismic reflection data in the acoustic approximation: *Geophysics*, **49**, no. 08, 1259–1266.
- Thorson, J. R., and Claerbout, J. F., 1985, Velocity stack and slant stochastic inversion: *Geophysics*, **50**, no. 12, 2727–2741.
- Tsai, C. J., 1985, Use of autoconvolution to suppress first-order long-period multiples: Use of autoconvolution to suppress first-order long-period multiples: *Soc. of Expl. Geophys., Geophysics*, 1410–1425.
- Ursin, B., 1990, Offset-dependent geometrical spreading in a layered medium (short note): *Geophysics*, **55**, no. 04, 492–496.
- van Borstelen, R., 2003, Optimization of marine data acquisition for the application of 3D SRME: *in 73rd Ann. Internat. Mtg Soc. of Expl. Geophys.*, 1965–1968.
- van Dedem, E., and Verschuur, D., 2002, 3D surface-related multiple prediction using sparse inversion: experience with field data: *Soc. of Expl. Geophys., 72nd Ann. Internat. Mtg*, 2094–2097.
- Verschuur, D. J., Berkhout, A. J., and Wapenaar, C. P. A., 1992, Adaptive surface-related multiple elimination: *Geophysics*, **57**, no. 09, 1166–1177.
- Wang, J., Kuehl, H., and Sacchi, M. D., 2003, Least-squares wave-equation avp imaging of 3D common azimuth data: *in 73rd Ann. Internat. Mtg Soc. of Expl. Geophys.*
- Wang, Y., 2003, Multiple subtraction using an expanded multichannel matching filter: *Geophysics*, **68**, no. 1, 346–354.
- Wiggins, J. W., 1988, Attenuation of complex water-bottom multiples by wave equation-based prediction and subtraction: *Geophysics*, **53**, no. 12, 1527–1539.
- Yu, J., and Schuster, G., 2001, Crosscorrelogram migration of IVSPWD data: *Soc. of Expl. Geophys., 71st Ann. Internat. Mtg*, 456–459.